Polymer 50 (2009) 1939–1947

Contents lists available at ScienceDirect

Polymer

journal homepage: www.elsevier.com/locate/polymer

Linking structure and nanomechanical properties via instrumented nanoindentations on well-defined and fine-tuned morphology poly(ethylene)

Tranchida Davide D.[a,*,1], Bartczak Zbigniew[b], Bielinski Dariusz[c], Kiflie Zebene[a,2], Galeski Andrzej[b], Piccarolo Stefano[a]

[a] Dipartimento di Ingegneria Chimica dei Processi e dei Materiali, Viale delle Scienze, University of Palermo, Palermo & INSTM Udr Palermo, Italy
[b] Centre of Molecular and Macromolecular Studies, Polish Academy of Sciences, Sienkiewicza 112, 90-363 Lodz, Poland
[c] Institute for Dye Technology, Technical University of Lodz, Zeromskiego 116, 90-924 Lodz, Poland

ARTICLE INFO

Article history:
Received 3 September 2008
Received in revised form
4 February 2009
Accepted 22 February 2009
Available online 26 February 2009

Keywords:
Nanoindentation
Morphology
Mechanical properties

ABSTRACT

Several poly(ethylene) samples with a broad range of morphologies were studied in this work using nanoindentations. The samples had degrees of crystallinity ranging from 30 to 100% while their Young's modulus ranged from few tens of MPa up to several GPa. Experimental conditions for the correct evaluation of Young's modulus were at first identified, choosing a suitable loading rate in order to minimize viscoelastic effects on the unloading. The force curves, i.e., plots of applied load vs. penetration depth, were then analyzed following two common procedures available in the literature. None of these procedures leads to satisfying results when compared to other experimental techniques. However, it was found that a recently proposed correction factor to the Oliver and Pharr procedure allows to evaluate reliably Young's modulus of the poly(ethylene) samples exhibiting very different, fine-tuned morphologies.

1. Introduction

Microindentation tests have been widely used in the past to characterize the local mechanical properties of complex materials like, for instance, semicrystalline polymers [1–5] or biological samples like cartilage [6–8], teeth [9] and bones [10,11]. Mechanical properties of polymers on microscale have been successfully linked to their structure, macroscopic creep behaviour and Young's modulus [1–5]. Also, in the case of biological samples, tissue mechanics has been related to disease progression or tissue repair.

The use of nanoindentation for nanoscale mechanical characterization of polymers is hampered by the principal assumption of most theories that the behaviour of the material during unloading is elastic only, while actually for most polymers and testing conditions it is strongly influenced by viscoelasticity [12]. The most remarkable phenomenon caused by viscoelasticity, observed especially in nanoindentation tests at low loading rate or with too short holding time, is the formation of a "nose" in the force curve, indicating an eventual increase in depth even during the unloading portion of the force curve.

Oliver and Pharr [13], O&P in the following, and Hochstetter et al. [14] proposed an alternative procedure which, starting from Sneddon's results [15], allowed to estimate Young's modulus without calibrations but taking into account a tip defect parameter. The use of high loading rates allowed them to minimize the effect of viscoelasticity and to evaluate reliably Young's modulus of polycarbonate and poly(diethylene glycol-bis-allyl carbonate) [14].

Baltà-Calleja and co-workers extensively studied in the past the mechanical behaviour during microindentations of a broad range of poly(ethylene) samples 1–5, characterized by chain-folded and chain-extended morphologies. In particular, microhardness was related to the microstructure [2], to creep behaviour [3], to plastic and elastic properties [4] and to glass transition [5].

The aim of this paper was to link the mechanical properties of the semicrystalline polymeric material with its microstructure through nanoindentation experiments. Polyethylene (PE) was chosen as the object of study in this work, due to the sufficient amount of knowledge that is already developed about its deformation mechanics and the possibility that the material offers to differentiate its structure and morphology in a broad range. A further insight into processes taking place during deformation of PE

* Corresponding author.
E-mail address: tranchid@mpip-mainz.mpg.de (D.D. Tranchida).
[1] Current address: Max-Planck-Institute for Polymer Research, Ackermannweg 10, 55128 Mainz, Germany.
[2] Current address: Chemical Engineering Department, Faculty of Technology, Addis Ababa University, P.O. Box 385, Addis Ababa, Ethiopia.

0032-3861/$ – see front matter © 2009 Elsevier Ltd. All rights reserved.
doi:10.1016/j.polymer.2009.02.032

is also offered by recent experiments performed in both tension [16] and compression [17–20] geometries.

The samples of fine-tuned morphology with the resulting degree of crystallinity were prepared by slight modifications of solidification conditions. The degree of crystallinity varied in a broad range, from 30% up to 100%, and with six different samples only in the range 60–80%. This implies that a high sensitivity of the procedure is needed in order to correctly discriminate between Young's modulus of these samples.

The results from the application of the O&P and the Hochstetter et al. procedures were analyzed and compared to the results obtained from a recently proposed [21] modification of the O&P procedure. This modification introduced a correction factor based on a calibration with a polymer sample of known elastic modulus, thus overlooking the effect of viscoelasticity.

2. Experimental

2.1. Materials

The materials used in this study (see Table 1) were various grades of commercial polyethylene, including three linear high-density polyethylenes (HDPE) of various molecular masses, and a random copolymer of ethylene with octene-1 (8.2 mol% of octene-1).

2.2. Sample preparation

Samples with chain-folded crystals were prepared by compression moulding at the temperature of 195 °C and pressure of 5 MPa between microscopic glass slides in order to obtain samples with flat and smooth surfaces suitable for nanoindentation tests. The compression moulded sheets were solidified either by fast cooling (quenching) in the iced water or by isothermal crystallization at 110 °C in order to obtain samples with conventional chain-folded crystals of various lamellar thickness and crystallinity.

Samples containing chain-extended crystals were prepared in a high pressure cell, and details of the experimental setup are given elsewhere [19,22].

2.3. DSC

The thermal analysis of the samples was conducted using a TA 2920 DSC apparatus (TA Instruments), calibrated with Indium. The melting thermograms were recorded at the heating rate of 10 °C/min, under nitrogen flow.

2.4. SAXS

Lamellar structure was probed by two-dimensional small angle X-ray scattering (2-D SAXS). The 0.5 m long Kiessig-type camera was equipped with a tapered capillary collimator (XOS) combined with additional pinholes (300 μm in diameter) forming the beam, an imaging plate as a detector and recording medium (Fuji). The camera was coupled to an X-ray source (sealed-tube, fine point CuK_α Ni-filtered radiation, operating at 50 kV and 40 mA; Philips). The collection time of the pattern was usually around 2 h. Exposed imaging plates were read with Phosphor Imager SI scanner and ImageQuant software (Molecular Dynamics). Long periods were determined from one-dimensional sections of 2-D pattern. Background and Lorentz corrections were applied to the curves. Long period was then calculated from the positions of the maximum of the corrected curves using the Bragg law.

Table 1
Molecular characteristics of the polymer studied.

Sample code	Manufacturer	M_w	M_w/M_n	Number of branches (1/1000C)	Melt flow rate (2.16 kg, 190 °C) (g/10 min)	Density (g/cm^3)
1	Quantum	57 000	3.5	<0.1	6.7	0.957
2	BASF	183 000	7.2	<0.2	0.2	0.956
3	BASF	478 000	12.2	<3	–	0.953
4	Exxon	82 000	3.7		3.0	0.902

2.5. SEM

For evaluation of the morphology of extended chain samples, the specimens were first prepared by cutting with an ultramicrotome in order to expose a flat and smooth cross-section surface. That surface was then etched with permanganic etchant mixture according to the procedure developed by Olley and Bassett [23], coated with fine layer of gold (ca. 20 nm thick) by ion sputtering device (Jeol JFC-1200) and then examined with a scanning electron microscope (Jeol JSM 5500LV).

2.6. Nanoindentations

A commercial nanoindentation system (Micro Materials NanoTest) was used with a Berkovich indenter and a spherical indenter of 5 μm nominal radius. The Berkovich indenter shape was also imaged by SEM in order to check against possible defects and/or tip rounding (due to, for example, wear or production scattering) which could complicate the analysis of the force curves. Indentations have been performed in a wide range of experimental conditions. Five loading rates (0.01, 0.03, 0.1, 0.3, 1 mN/s) and four different loads (0.25, 0.5, 0.75, 1 mN) were used in order to test the effect of the time scale and the amount of deformation on the evaluation of the elastic modulus. All tests were performed at room temperature, and a 30 s holding period was used at maximum load between loading and unloading stages, to minimize the effect of viscoelasticity on the unloading curve. Moreover, in order to assess the thermal drift, an additional hold at 90% unloading was applied in all tests, which was subsequently subtracted from the force curve. The indenter area function, i.e., the relation between the contact area and the contact depth as evaluated from the force curve, was calibrated on fused silica. The methods used to analyze the force curves, i.e., plots of applied load vs. penetration depth, will be discussed in the following sections.

3. Results and discussion

3.1. Sample characterization

The samples obtained by crystallization at various conditions were first characterized by DSC, SAXS and SEM, as reported in the Experimental part. Results are presented in Table 2, along with the sample codes used in the following. It can be seen that a fine tuning of the degree of crystallinity developed upon crystallization was obtained, with two extreme cases: 30 wt.% and 100 wt.% for Q-4 and CE-1, respectively, and 6 samples within the range of 60–80%.

SEM observations showed that all samples of the H and Q series, crystallized at atmospheric pressure, had spherulitic morphology with spherulites completely filled with thin chain-folded lamellae. In contrast, randomly oriented and very thick lamellae were observed in CE samples, crystallized at the high pressure of 488 MPa. The thickness of these lamellae frequently exceeded 1 μm, indicating the chain-extended morphology of the crystals. Typical morphology of the samples studied is illustrated in Fig. 1.

Table 2
Crystallinity degree for the samples prepared under different solidification conditions from the materials listed in Table 1 and properties of crystalline phase.

Sample code[a]	Melting temperature, T_m[b] (°C)	Weight crystallinity, X_c[b] (wt.%)	Volumetric crystallinity, X_v[c] (vol.%)	Crystalline stem length, l^*[d] (nm)	Long period, LP (nm)	Lamellar thickness, L_t[e] (nm)
H-1	131.0	80	77.3	17.7	27.5	21.3
H-2	131.7	76.6	73.6	18.7	28.5	21.0
H-3	132.0	67.9	64.3	19.1	27.8	17.9
Q-1	130.6	64.0	60.2	17.3	20	12.0
Q-2	130.6	69.2	65.6	17.3	20.6	13.5
Q-3	131.0	60.6	56.7	17.7	21.3	12.1
CE-1	144.1	100	100	n.a.	n.a.	600*
CE-2	142.7	100	100	n.a.	n.a.	530*
CE-3	146.0	96.0	95.3	n.a.	n.a.	410*
Q-4	94.7	30	26.7	5.1	11.5	3.1

[a] Q: quenched in iced water, H: isothermally crystallized at 110 °C, CE: extended chain, crystallized isothermally at 247 °C and 488 MPa.
[b] Determined from the DSC melting data.
[c] Calculated from X_c.
[d] The stem length, l^*, determined from DSC.
[e] The lamellar thickness was evaluated either from long period and X_v (chain-folded samples) or as average values from direct SEM observations (extended chain samples; marked with an asterisk).

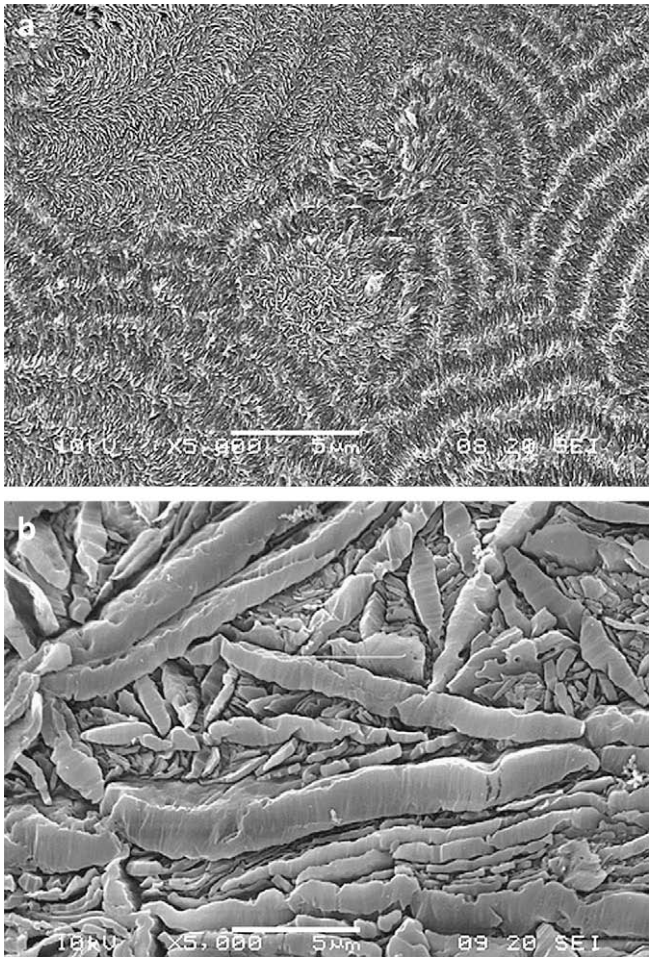

Fig. 1. SEM micrographs illustrating typical morphologies of the samples studied: (a) banded spherulites in sample H-2, crystallized isothermally at 110 °C under atmospheric pressure; (b) chain-extended crystals of sample CE-2 crystallized at $T = 247$ °C and $p = 488$ MPa. Scale bar of 5 μm on both micrographs.

3.2. Preliminary analysis

Fig. 2 shows four randomly selected force curves, obtained at 0.1 mN/s loading rate and the peak load of 0.5 mN for samples exhibiting different morphology and crystallinity. It is apparent from these curves that nanoindentation scales correctly the rigidity of samples, i.e., an increasing penetration depth is observed with decreasing degree of crystallinity. It can also be appreciated even by an eye, that the contact stiffness, which is related to Young's modulus, is correctly larger for the samples with higher degree of crystallinity, as it will be discussed in detail in the following.

The presented curves illustrate clearly a dramatic influence of the amorphous content. An increase of the amorphous content by 40% when going from CE-1 ($X_c = 100$ wt.%) to the Q-3 sample ($X_c = 60$ wt.%) leads to a significant increase of the penetration depth, which is roughly doubled. However, this change is much smaller when compared to that between the Q-3 and Q-4 samples ($X_c = 60$ wt.% and 30 wt.%, respectively). In this case, a smaller increase of amorphous content (by 30%) results in an increase of the penetration depth by more than three times. It was already shown for the same materials as used in this work that the amount of the amorphous fraction is the principal parameter controlling Young's modulus [17]: an increase of the amorphous content results in significant and monotonic decrease of the modulus. On attributing such changes to the overall content of the amorphous phase, one should recognize the different scale of the contact, above a hundred of nm, with respect to the thickness of lamellae. Already the interaction of few lamellae with an indenter turns the material response to that of bulk [24].

Following Crist et al. [25], one can rationalize the substantial dependence of the modulus on phase structure as being a result of the strong dependence of the modulus of the amorphous phase on crystal thickness, through modification of the α mechanical relaxation process in the vicinity of the interface in addition to mixing rules combining moduli of component phases. For small lamellar thickness and relatively thick amorphous layers as in the Q-4 sample (cf. Table 2), a low elastic modulus of the amorphous phase in the order of few MPa can be expected. On the other hand, it was postulated that for highly crystalline samples, demonstrating very narrow amorphous layers, the modulus of the amorphous phase can increase up to relatively high values (approx. 300 MPa [25]) due to the influence of adjacent crystalline layers such that the α mechanical relaxation process becomes hindered. This can explain the noticeable differences in the contact stiffness, or equivalently in Young's modulus, as well as the differences in

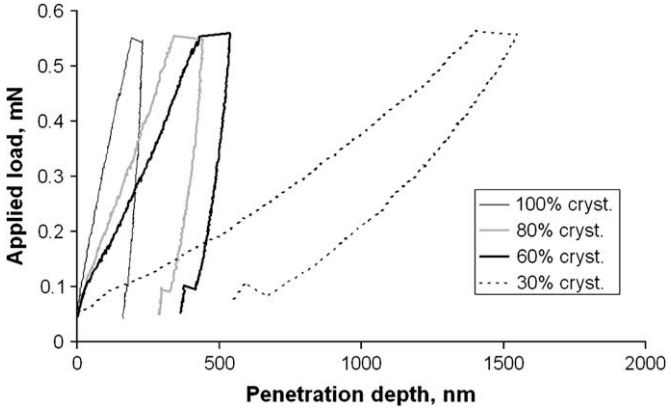

Fig. 2. Representative force curves obtained on PE samples with different degree of crystallinity, showing the dramatic changes in mechanical properties arising from differences in the morphology.

maximum penetration depth qualitatively observed among the samples presented in Fig. 2.

The proper experimental conditions, which allow to minimize the viscoelastic effects, should be identified before switching to quantitative analysis of the force curves and evaluation of Young's modulus. Nanoindentation tests performed at different loading rates can result in very different mechanical responses [13]. This can be illustrated by the exemplary data of the maximum penetration upon loading obtained for sample Q-3, 60.6 wt.% X_c, during nanoindentations performed in a wide range of applied loads and loading rates, shown in Fig. 3. Similarly, it can be expected that the choice of the unloading rate also greatly influences the subsequent evaluation of Young's modulus.

The trend of the maximum penetration depth, that decreases with increasing loading rate, observed in Fig. 3 follows a power law curve, with the exponent of approximately −0.08 when penetration is given in nm and loading rate in mN/s. Moreover, 'nanohardness' may be defined as the mean contact pressure which is directly proportional to the applied load and inversely proportional to the square of the penetration depth, through a constant related to the geometry of the indenter. This means that 'nanohardness' in MPa is related to the loading rate, in mN/s, also through a power law relationship, with an exponent of nearly 0.16. This result can be compared to the work of Baltà-Calleja et al. [3], who showed that the microhardness of several PE chain-folded samples decreased with increasing loading time (or, equivalently, with decreasing loading rate) following a power law with the exponent of 0.1. Therefore, a comparable effect of viscoelasticity was found on both nano- and microindentation scales, although the slight difference in the two exponent values deserves a further comment: it should be noted that the meaning of 'nanohardness' is different from the commonly used microhardness, since the former is a quantity determined by instrumented indentation tests under full load and the latter is obtained from the residual imprint left behind the indenter on the unloaded sample. Therefore 'nanohardness' is clearly related not only to the plastic properties of the material, as microhardness is, but also to its elastic properties and this is accounted by the remarkable recovery on unloading shown in Fig. 2. Moreover, Fig. 3 shows a different dependence of penetration depth on loading rate, i.e., experimental time, at different applied loads. This might be interpreted as a non-linear viscoelastic phenomenon, but it is actually an artefact that originated from the different levels of penetration depth attained. Indeed, the same information in Fig. 3 is reported in Table 3 about the H-3 sample as

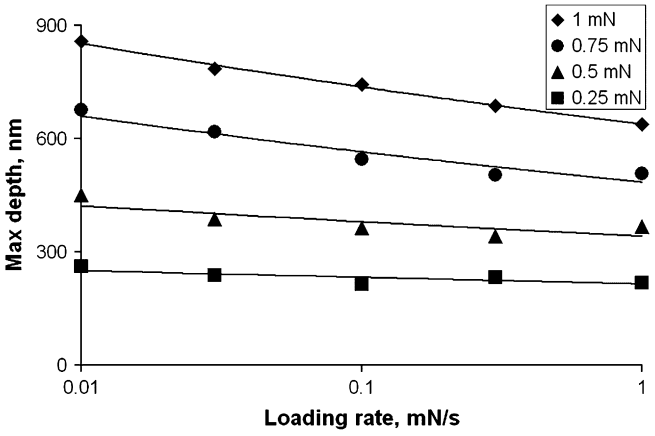

Fig. 3. Maximum depth, as registered from the force curves, obtained at different maximum load levels and with loading rate varying in a broad range for the sample H-3 ($X_c = 67.9$ wt.%).

Table 3
Ratio of the maximum depth at each loading rate to the penetration depth at the lowest loading rate, 0.01 mN/s, determined for sample H-3.

L (mN)/L' (mN/s)	0.01	0.03	0.1	0.3	1
0.25	1	0.91	0.82	0.89	0.83
0.5	1	0.86	0.81	0.76	0.81
0.75	1	0.91	0.81	0.75	0.75
1	1	0.92	0.87	0.80	0.74

the ratio of maximum depth at each loading rate normalized by the penetration depth at the lowest loading rate, 0.01 mN/s. Although the dependence on loading rate is preserved, it can be noted that the dependence on applied load is much less significant than Fig. 3 might suggest, thus invoking non-linear viscoelastic phenomenon might be debatable and further confirming that the indentation response of polymers at sufficiently high loading rates is dominated by short term recoverable mechanisms [26].

Fig. 4 presents another feature of PE samples probed by nanoindentation. It shows a typical dependence of the contact compliance, i.e., the reciprocal of the unloading slope, on the degree of crystallinity, determined from nanoindentation force curves, obtained at the loading rate of 0.3 mN/s. Similar to Fig. 2 the different mechanical behaviour of the samples of various morphology and crystallinity is clearly outlined. The difference between the behaviour of Q-3 ($X_c = 30$ wt.%) and Q-4 ($X_c = 60.6$ wt.%) is again larger than that between the Q-4 and the CE-1 ($X_c = 100$ wt.%) and the discussion made in relation to Fig. 2 actually applies in this case as well.

Recently, Cheng and Cheng [27] based on numerical simulations reported that a limiting value for the initial unloading slopes is obtained when the loading rate becomes high enough so that the effect of viscoelasticity is minimized. The results obtained in this study suggest that the loading rate of 0.3 mN/s can be considered as such a limiting rate, high enough to minimize viscoelastic effects in the studied polyethylene samples.

3.3. Holding

It can be recalled from Fig. 2 that penetration increases during the holding period, i.e., while the load is kept constant after the loading step and before unloading. It was also shown that penetration depth, in addition to its time dependence, is proportional to the square root of the applied load.

Although one should expect for each different morphology studied in this work that the contribution from the time-dependent

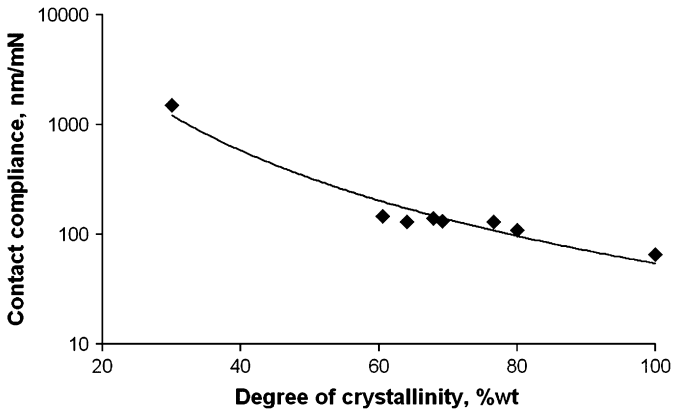

Fig. 4. Contact compliance, measured as the opposite of the unloading curve slope, scales well with the samples' crystallinity fraction used.

term would be the same during tests performed at different loads, and the square root of applied load to be proportional to the final penetration depth, the results obtained reveal different behaviour. For samples with similar morphologies, i.e., crystallinity in the range 60–80%, the exponent relating applied load and final penetration depth, although different from 0.5, was found to be constant. In particular, this exponent was found to be loading rate dependent with a value of 0.14 ± 0.08 in the case of very low indentation rate, and 0.3 ± 0.04 when the highest loading rate was used.

Fig. 5 shows a typical dependence on loading rate of the amount of creep taking place during the holding period observed on sample Q-3. The creep data were normalized to the final penetration depth reached under loading. As expected considering the relaxation process during the loading process, at low loading rates the amount of 'creep' is low and limited to nearly 20% of the maximum depth. In contrast at high loading rates the penetration depth during holding amounts to as much as the penetration obtained during loading. These findings confirm observations already reported in the literature [13,14] that a high loading rate is needed to limit relaxation phenomena.

As far as the holding part of the indentation experiment is concerned, the dependence of penetration depth on time can be analyzed according to a recently proposed phenomenological approach [28]. The fitted curve captures well the shape of the creep curve, and this allows to link the creep behaviour to material properties, which in turn are related to the molecular characteristics and sample morphology [28]. The normalized increase of depth is plotted against $(\text{time} + 1)$ and the experimental creep data are fitted with an equation of the form of $k \ln(\text{time} + 1)$. The only fitting constant k, a sort of creep parameter, can be related to the morphology and to the loading history, as illustrated in Fig. 6, where the parameter k is plotted against the amount of amorphous content for two different loading rates.

The creep parameter, k, at high loading rate can be related to the amount of amorphous phase which can be considered as a continuous molecular network of highly entangled chains [18]. Physical cross-links, due to entanglements and crystallites adjacent to the amorphous layers, confer stiffness when the initial fast deformation is applied. However, they are prone to subsequent creep when a constant load is applied for a relatively long time. This leads to a linear dependence of the fitting parameter k on crystallinity, as is clearly shown in Fig. 6.

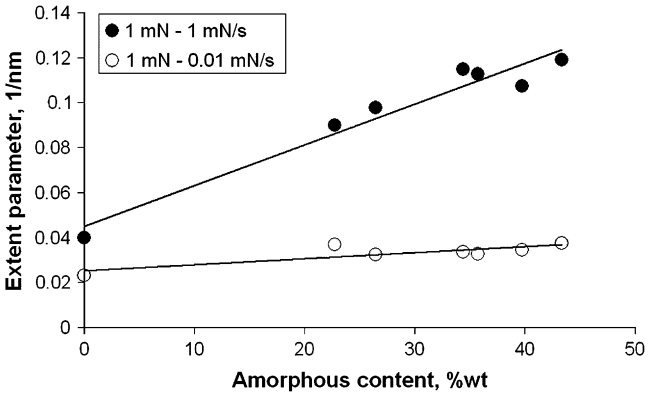

Fig. 6. Creep extent parameter, fitted according to Fig. 5, plotted against samples' amorphous content. The plot shows that creep is low for low loading rates, i.e., the material has more time to relax during loading, while creep is much more significant for fast nanoindentations.

At low loading rate, i.e., when the sample relaxes during loading, the creep extent depends on the sample crystallinity to a much lower degree (see Fig. 6), although a similar linear dependence of k on crystallinity can still be found. This observation also implies that crystallinity or more precisely, amorphous content, determines the viscoelastic behaviour and it is quantitatively accessible during the holding if and only if the loading time is short enough (i.e., loading rate is sufficiently high) with respect to the relevant relaxation time of the material.

3.4. Unloading curve

Oliver and Pharr procedure. Contact compliance in Fig. 4 can be converted into Young's modulus according to the well-known O&P approach [13,29], as shown in Fig. 7. The O&P procedure can correctly discriminate very different morphologies, and therefore it seems to be suitable for a comparison of different samples. The 30% crystalline sample (Q-4), for example, is much more compliant than the samples in the range of 60–80% crystallinity, which in turn are more compliant than the 100% crystalline samples (CE-1, CE-2). However, the inset in Fig. 7 apparently shows that the estimated values of the Young moduli for samples within the crystallinity range of 60–80 wt.% are affected by considerable scatter. This indicates that the mechanical properties of these samples were not

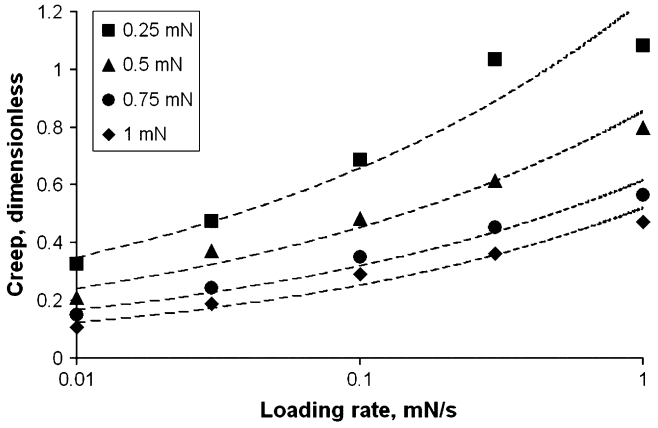

Fig. 5. The creep extent, measured as the ratio of penetration depth during holding and maximum penetration depth reached under loading, strongly depends on the loading rate used. This plot refers to the sample Q-3, while a generalization is given in Fig. 6.

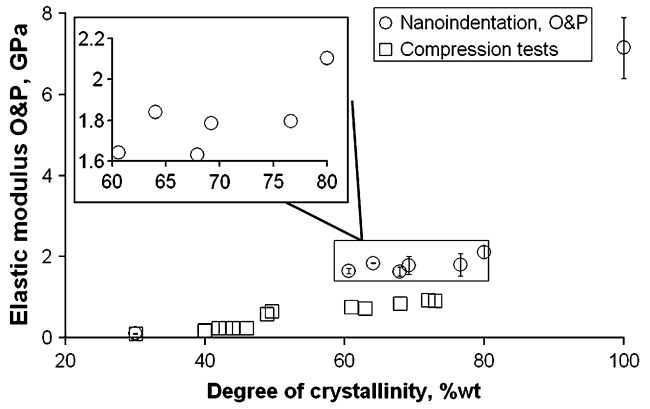

Fig. 7. Young's modulus evaluated with the Oliver and Pharr procedure from nanoindentation data (circles) compared with the results of compression tests (squares). Inset shows a scatter of nanoindentation-based modulus estimates obtained for samples of narrower morphological differences.

captured accurately enough with the O&P approach. What is however more relevant is that the absolute values of the elastic moduli are systematically larger than those obtained from macroscopic compression test [17], also shown in Fig. 7 for comparison. Obviously, the geometries of the nanoindentation and compression tests are different, and a constraining effect of the material surrounding the indent might be expected to increase the apparent modulus when probed by nanoindentation [13]. Even accounting of the different geometries, the nearly 100% difference between the moduli obtained from compression and those from nanoindentation data is definitely too large. The material surrounding the deformation zone acts as a constraint however the constraining effect, obviously dramatic in the case of an incompressible material or in the case of full confinement, plays a partial role during a nanoindentation test since the material around the indentation can, to some extent, deform [30]. Therefore, the large overestimation of the modulus by the O&P method most probably originates from other sources.

In our opinion the failure of the O&P procedure is rather related to the onset of viscoelastic contributions taking place during the unloading portion of the force curve [30]. Albeit minimized by the high unloading rates applied in our experiments and being altogether neglected in the contact mechanics model, they still play a significant role in determining the deviations observed. The O&P procedure stems from Sneddon's model, which suggests a power law relationship between applied load and penetration depth for elastic contact, i.e., on unloading. The exponent is bounded between 1 and 2 depending on the indenter geometry, i.e., for the flat punch and the cone, respectively. In the case of the PE samples studied in this work, the exponent estimated was instead always greater than 4.

Hochstetter et al.'s procedure. The procedure described by Hochstetter et al. [14] makes use of Sneddon's model, similarly to the O&P procedure, albeit introducing some modifications in the procedure. Rather than calibrating the area function, they introduce an 'apparent tip defect' length, related to tip rounding, modifying the ideal shape of the Berkovich indenter.

Fig. 8 presents Young's moduli, estimated from experimental nanoindentation force curves on the basis of Hochstetter et al.'s procedure for the samples studied in this work. Again, Young's moduli obtained from nanoindentations are compared with the set of values obtained in macroscopic compression tests [17]. A significant improvement is clearly observed with respect to the moduli obtained by the O&P procedure, as shown in Fig. 7. The absolute values of modulus are now on the same scale as those from compression tests, although a significant scatter, similar in magnitude to that reported in the inset of Fig. 7, can be still observed. A further improvement is that the dependence of modulus on crystallinity, presented in Fig. 8, shows a trend closely following the compression data.

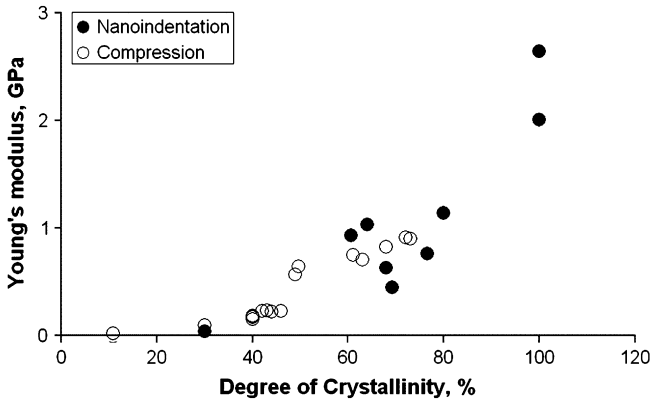

Fig. 8. Young's modulus evaluated with the Hochstetter et al. procedure from nanoindentation data (filled circles) compared with the results of compression tests (open symbols).

Table 4
Tip defect values as obtained from the procedure of Hochstetter et al., also compared to the degree of crystallinity and Young's moduli of the samples as measured by compression tests.

Sample	Degree of crystallinity (wt.%)	Tip defect (nm)
CE-2	100	384
H-1	80	325
H-2	76	658
Q-2	69	1372
H-3	68	740
Q-1	64	370
Q-3	60	349
Q-4	30	1632

Unfortunately, also this procedure shows some serious flaws as pointed out in Table 4. According to this model the tip defect parameter should be related to the geometry of the indenter solely, being therefore independent of the material under test. The data presented in Table 4 clearly contradict this hypothesis since the tip defect parameter changes from one sample to another thus becoming a purely fitting parameter and losing the physical meaning as attributed by the procedure [14]. One may also argue that the values of the tip defect parameter, h_0, might depend on the penetration depth achieved during the test, implying a different effect of tip roundness on the geometry of the contact and in turn implying that, at constant maximum applied load, they should depend on the elastic moduli. However, it can be observed that h_0 is not scaled with the bulk Young's moduli obtained from compression tests. Furthermore, the tip defect values can be seen to be too large when compared to the SEM image of the indenter used in the present study, not shown here.

Tranchida et al. correction factor. A phenomenological correction factor, χ, was recently added to the Oliver and Pharr procedure by Tranchida et al. [21]. In the case of the study reported here, sample Q-3, which has a degree of crystallinity midway among the samples investigated, was chosen as the reference on which the χ factor was calibrated based on a series of force curves obtained at various loading conditions, according to the equation:

$$\chi = 1 + ah^b/E \tag{1}$$

where E is the elastic modulus, in GPa, common to all force curves and assumed to be known only for this sample, h is penetration depth, in nm, in a given force curve. The constants a and b obtained from this sample are equal to 1825.6 and −1.2479, respectively. It is worth to remember that these values are specific for the particular indenter with all its peculiarities: flaws, scratches, geometry (e.g. Berkovich in this case), etc. This procedure allows to overcome the increasing error in elastic modulus evaluation for softer materials, as well as its penetration dependence [21].

Fig. 9 presents the data obtained with the O&P approach, already shown in Fig. 7, but now corrected with the χ factor determined on the basis of the modulus of sample Q-3, whose modulus is supposed to be a priori known [21]. The bulk moduli obtained from compression tests, also indicated in the same figure, show a satisfactory agreement with the results from nanoindentations and the dispersion is also seen to decrease. Even recalling the possible influence of confinement to the deformation, which could result in higher values of the modulus, one observes that this effect is only marginal, albeit in the correct direction, with respect to the absolute values. Indeed, elastic moduli drawn from

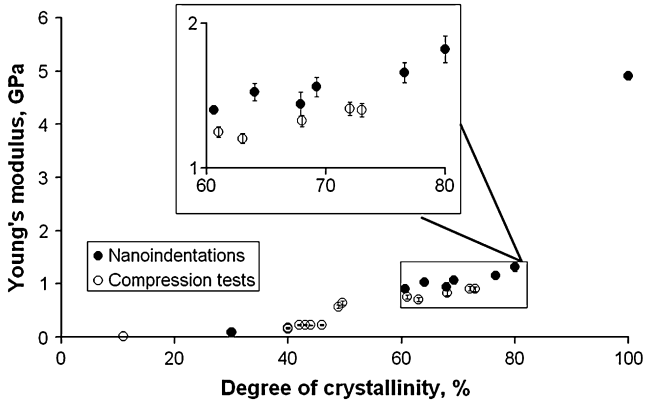

Fig. 9. Young's modulus values obtained from nanoindentations, as evaluated from the procedure described in Ref. [21] after a further calibration (filled circles), showing good agreement with values determined from compression tests (open circles). Inset illustrates a relatively good agreement of both nanoindentation and uniaxial compression data sets for samples of fine-tuned morphology and crystallinity.

this procedure are only slightly larger than those obtained from compression tests. Comparing the data presented in Fig. 9 with those of Figs. 7 and 8, one can conclude that the estimation of the elastic modulus of the samples studied on the basis of the nanoindentation tests is the most reasonable when the Oliver and Pharr approach together with the additional χ correction is applied to the experimental data (Fig. 9). The values of the elastic moduli determined from nanoindentation unloading data according to this procedure show a relatively low scatter and apparently give the best agreement with macroscopic compression tests' data, when compared to the results of other estimates.

3.5. Loading curve

In a previous work concerning nanoindentations [31], the authors showed that when testing mechanical properties on nanometer scale by Atomic Force Microscope, the mechanical response of polymers is essentially elastic. This behaviour was attributed to distinct and probably synergetic phenomena, one of the interests in this work being a size scale effect originating from the fact that the local stress might be very high but still on a volume smaller than the critical volume for yielding to take place [32]. For the geometry of DSI nanoindentations, one can easily calculate [32] that the maximum of the stress field in order to induce plasticity is less than 10% larger than the yield stress of the bulk sample. Therefore, it can be concluded that during DSI nanoindentations yielding takes place as soon as the yield stress is reached in one point of the stress field, in agreement with common yielding criteria, i.e., at relatively low loads during collection of a force curve.

Moreover, the stress field during a nanoindentation is three-dimensional and relatively quickly changing in space. This means that some volumes of the sample experience stresses above the yield point while some others are still in the elastic range. Therefore, it is difficult to define a situation represented by a stress or strain where yielding occurs. However, in analogy to standard macroscopic uniaxial tests, it is reasonable to assume that the first part of the force curve describes primarily an elastic behaviour and that a transition should be observed on the force curve when some volume of the sample begins to yield. It is worth to mention that this has been observed in the case of metals. However, the link between the load at which the sample begins to yield and the yielding point of polymers as measured in compression tests is not straightforward and is difficult to find.

Elastic contact models can indeed fit the very first part of the loading force curve. As the load increases and the deformation proceeds, yielding occurs and plastic deformation starts beneath the apex of the indenter, and an elastic–plastic model should be used to describe the respective portions of the force curve. The knowledge of the transition between these two regimes, elastic and elastic–plastic, could help to define the 'yielding force'. However, due to instrumental limitations in this work, a pre-load of 0.05 mN had always to be applied to the sample prior to the acquisition of the force curve. Although such a tiny pre-load has usually a negligible effect for metals or ceramics, it has to be appropriately taken into account when studying 'compliant' materials, like polymers. To do that, the original force curve was corrected by shifting it along the penetration depth axis with a distance corresponding to the penetration depth for the applied pre-load of 0.05 mN as predicted by Sneddon's model [15] for the case of the contact between an elastic half-space and a conical indenter with semi-opening angle of $\theta = 70°$, equivalent to the Berkovich indenter, used in this study. The remaining, 'post-yielding' part of the force curve was in turn fitted with an elastic–plastic model. Hays and Kendall [33] suggested to use Kick's law, relating applied load and penetration depth scaled by an exponent of 2, corrected by a constant term, denoted as W.

$$L = W + Kh^2 \tag{2}$$

The parameter W was suggested to be a purely Newtonian constant term, i.e., a small fraction of the total load that does not contribute to the indentation but acts as a reaction force of the specimen. This physical meaning actually fits with our experiments, since the shift introduced, to account for pre-load, for the elastic–plastic curve in Fig. 10, needed for a proper fitting of the force curve, is basically due to the occurrence of the first elastic contact.

The constant K was in this study evaluated according to Hainsworth et al. [34].

The procedure is illustrated in Fig. 10 for the sample H-1. The intersection between the two curves, elastic and elastic–plastic, can be interpreted as the yielding force on nanoindentation. It is, however, very difficult to estimate from it the respective stress since the actual area under load is not known.

The procedure described above was applied to the results obtained for samples studied in this work in order to estimate the yield force. The results are shown in Fig. 11, in which the yield force is plotted against the thickness of the lamellae of the respective

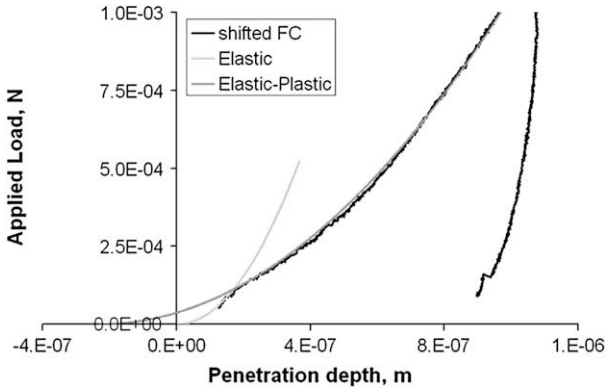

Fig. 10. Illustration of the modeling of the loading force curve. The thick black line is the experimental curve obtained for the sample H-1. The thin grey curve is the one predicted by Sneddon's model, assuming that the deformation in the initial range is purely elastic. The thick grey curve was fitted to the experimental curve following an elastic–plastic contact as described in Refs. [33,34].

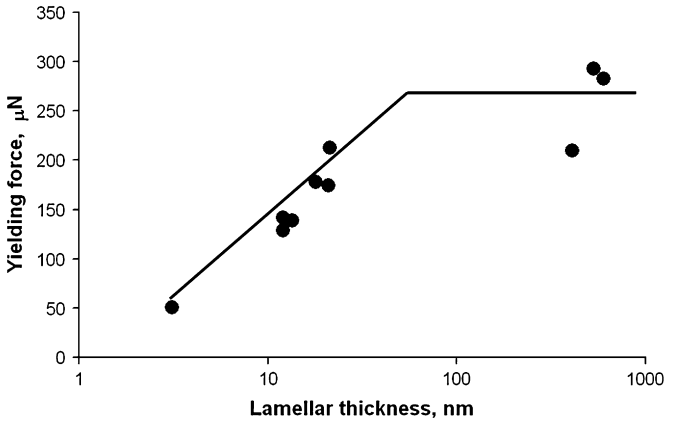

Fig. 11. The dependence of the yielding force, as estimated from the very first purely elastic part of the loading curve on the thickness of lamellae. The line drawn through data points does not represent any particular dependence and is only to guide an eye.

sample. It can be observed that the yield force increases initially with an increase of the thickness of lamellae and then saturates and levels off for larger thickness.

The initial increase of the yield force with increasing crystal thickness observed in Fig. 11 agrees with the results of Brooks and Mukhtar [35], who demonstrated that for polyethylene lamellar crystals of low and moderate thickness (3–28 nm thick) their yield stress increases with an increasing thickness due to variation in thermal nucleation of dislocations controlling the plastic deformation by crystallographic slip, which according to the model of Young [36] and Crist [37] is thickness-dependent. On the other hand, Kazmierczak et al. [19,20] demonstrated that, when the lamellar thickness increases above approximately 40 nm, the yield stress levels off and no longer depends on the thickness, since for sufficiently thick lamellae the crystallographic slip becomes controlled by the generation of dislocation half-loop from crystal side surfaces instead of by thermally generated screw dislocations in the bulk of that crystal. The generation of dislocation half-loops can operate only in the lamellae of sufficient thickness. This mechanism, however, once activated generates dislocations necessary for plastic deformation with the high rate, practically independent of lamellar thickness. This allows the crystal slip to proceed at the stress independent of crystal size and lower than the stress associated with the slip run by dislocations thermally generated in the bulk, actually increasing substantially with crystal thickness [20]. Therefore, in contrast to thin lamellae, the yield stress of lamellae thicker than approximately 40 nm does not depend on their thickness any longer [19,20]. Our data obtained for series of samples containing either thin chain-folded or much thicker chain-extended crystals, presented in Fig. 11, confirm the findings of Kazmierczak et al. [19] showing that for lamellae with thickness smaller than approximately 40 nm, the yield stress is controlled by the their thickness while for those thicker than 40 nm the yield does not depend on the crystal thickness.

4. Conclusions

The relationship between elastic moduli, as estimated from nanoindentation experiments, and morphology and resultant crystallinity of polyethylene samples with fine-tuned morphologies were studied in this work. A broad range of crystallinities, $X_c = 30$–100 wt.%, was obtained with 9 samples, 6 of which exhibited very similar morphologies and crystallinities in the range 60–80 wt.%.

A detailed analysis of three parts of the force curve: the loading, holding and unloading portions, was performed to extract the mechanical characteristics of the samples. It is worth to notice that although the size of the morphological features is comparable to the typical dimensions of the indenting probe, the samples can be considered as a continuum. Indeed, the loads used in this work were relatively high implying a large volume involved in the stress field, which mediates the contributions of crystalline lamellae and amorphous layers. Much lower loads and penetrations are required to identify the properties of component phases in a semicrystalline polymer; they are available only by AFM nanoindentations [38].

During holding, i.e., the portion of the force curve between loading and unloading, it was observed that the extent of creep does not scale with the square root of the applied load [39]. A relatively low creep level is observed when a low loading rate is used since the material can relax partially already during the loading time and enters into the holding stage almost relaxed. On the other hand, creep takes place to a large extent when high loading rates are adopted. As far as the dependence on morphological features is concerned, a phenomenologically defined creep parameter was seen to increase linearly with the amount of amorphous phase (i.e., the creep parameter decreases with increasing crystallinity).

Young's modulus was evaluated upon unloading by the procedures available in the literature showing an inconsistency of the models usually applied to non-viscoelastic materials. It was shown that the application of a semi-empirical correction resulted in a reasonably more accurate evaluation of Young's modulus and additionally allowed to discriminate between the mechanical behaviour of the samples of only slightly different morphology and crystallinity.

The transition between elastic and plastic regime during nanoindentation test and its influence on the loading curve were also studied. The very first part of the force curve was analyzed by Sneddon's elastic contact model [15], and the point at which the experimental curve departed from the theoretical curve was attributed to the yield point and the respective load to the yielding force. It is worth stressing that since the actual area under load is unknown the exact link between this yielding force value and the yield stress as measured by macroscopic tests is not clear. However, the yielding force was found to increase with crystal thickness at low and moderate thickness, similar to the yield stress during macroscopic tests [22]. With the lamellar thickness increasing above of ca. 40 nm, however, this linear dependence is lost for both nanoindentation yielding force and macroscopic yield stress. This transition is most probably related to the change of the control over crystallographic slip processes from thermal generation of dislocations in the bulk of the crystal to the generation of dislocation half-loop from crystal side surfaces, a mechanism which is independent of the crystal thickness [19]. Such a very similar behaviour of the yield force in nanoindentation and macroscopic yield stress suggest that both quantities are indeed tightly related to each other.

Acknowledgements

This work was partially funded by the European Science Foundation through a Short Term Scientific Mission in the framework of COST P12 Action, Structuring of Polymers, and the budget sources for science in the years 2005–2008 by the Ministry of Science of Poland as a research project (grant 3 T08E007 28).

References

[1] Baltà-Calleja FJ. Adv Polym Sci 1985;66:117–48.
[2] Flores A, Baltà-Calleja FJ, Bassett DC. J Polym Sci Part B 1999;37:3151–8.
[3] Baltà-Calleja FJ, Flores A, Ania F, Bassett DC. J Mater Sci 2000;35:1315–9.
[4] Flores A, Baltà-Calleja FJ, Attenburrow GE, Bassett DC. Polymer 2000;41:5431–5.
[5] Fakirov S, Krasteva B. J Macromol Sci Phys 2000;B39:297–301.

[6] Zheng YP, Mak AFT, Leung AKL. J Rehabil Res Dev 2001;38:487–504.
[7] Setton LA, Mow VC, Muller FJ, Pita JC, Howell DS. J Orthop Res 1994;12:451–63.
[8] Athanasiou KA, Rosenwasser MP, Buckwalter JA, Malinin TI, Mow VC. J Orthop Res 1991;9:330–40.
[9] Kinney JH, Marshall SJ, Marshall GW. Crit Rev Oral Biol Med 2003;14:13–29.
[10] Riches PE, Everitt NM, McNally DS. J Biomech 2000;33:1551.
[11] Rapoff AJ, Rinaldi RG, Hotzman JL, Daegling DJ. Am J Phys Anthropol 2008;135:100–9.
[12] Tranchida D, Piccarolo S. Macromol Rapid Commun 2005;26:1800–4.
[13] Oliver WC, Pharr GM. J Mater Res 1992;7:1564–83.
[14] Hochstetter G, Jimenez A, Loubet JL. J Macromol Sci B Phys 1999;38:681–92.
[15] Sneddon IN. Int J Eng Sci 1965;3:47–57.
[16] Hiss R, Hobeika S, Lynn C, Strobl G. Macromolecules 1999;32:4390–403.
[17] Bartczak Z, Kozanecki M. Polymer 2005;46:8210–21.
[18] Bartczak Z. Polymer 2005;46:10339–54.
[19] Kazmierczak T, Galeski A, Argon AS. Polymer 2005;46:8926–36.
[20] Argon AS, Galeski A, Kazmierczak T. Polymer 2005;46:11798–805.
[21] Tranchida D, Piccarolo S, Loos J, Alexeev A. Appl Phys Lett 2006;89:171905.
[22] Bartczak Z. Macromolecules 2005;38:7702–13.
[23] Olley RH, Bassett DC. Polymer 1982;23:1707–10.
[24] Tranchida D, Kiflie Z, Piccarolo S. Macromolecules 2007;40:7366–71.
[25] Crist B, Fisher CJ, Howard PR. Macromolecules 1989;22:1709–18.
[26] Tranchida D, Piccarolo S. Polymer 2005;46:4032–40.
[27] Cheng YT, Cheng CM. J Mater Res 2005;20:1046–53.
[28] Beake B. J Phys D Appl Phys 2006;39:4478–85.
[29] Oliver WC, Pharr GM. J Mater Res 2004;19:3–20.
[30] Tranchida D, Piccarolo S, Loos J, Alexeev A. Macromolecules 2007;40:1259–67.
[31] Tranchida D, Piccarolo S, Soliman M. Macromolecules 2006;39:4547–56.
[32] Bushby AJ, Dunstan DJ. J Mater Res 2004;19:137–42.
[33] Hays C, Kendall EG. Metallurgy 1973;6:275–82.
[34] Hainsworth SV, Chandler HW, Page TF. J Mater Res 1996;11:1987–95.
[35] Brooks NWJ, Mukhtar M. Polymer 2000;41:1475–80.
[36] Young RJ, Bowden PB, Ritchie JM, Rider JG. J Mater Sci 1973;8:23–36.
[37] Crist B. Polym Commun 1989;30:69–71.
[38] Tranchida D, Kiflie Z, Piccarolo S. Macromol Rapid Commun 2006;27:1584–9.
[39] Fischer-Cripps AC. Mater Sci Eng A 2004;385:74–82.